Journal of Applied Fluid Mechanics, Vol. 11, No. 3, pp. 755-764, 2018.
Available online at www.jafmonline.net, ISSN 1735-3572, EISSN 1735-3645.
DOI: 10.29252/jafm.11.03.28343

Flow Simulation of Various Riblet Shapes and a Uniform Model for Boundary Layer

Y. Yu, X. Ren, X. Li† and C. Gu

Key Laboratory for Thermal Science and Power Engineering of Ministry of Education, Department of Energy and Power Engineering, Tsinghua University, Beijing 100084, PR China

†*Corresponding author Email: xs-li@mail.tsinghua.edu.cn*

(Received August 25, 2017; accepted December 7, 2017)

ABSTRACT

Various riblet shapes are simulated through the computational fluid dynamics method for the elucidation of riblet effects on turbulent boundary layers and skin friction reduction. For the different shapes, seven typical riblet models are investigated by using renormalization group k-epsilon turbulence models. Simulation results are consistent with the existing theoretical data regarding flat plate and experimental results obtained from the riblet shapes. The riblet velocity profiles cannot satisfy the existing von Kármán's constants in the logarithmic law boundary layer. The slope and intercept of the logarithmic law are strongly affected by geometric parameters and riblet shapes, and the effect of geometric parameters can be modeled. Meanwhile, the effects of riblet shapes can be modeled with a shape factor composed of a nondimensional cavity ratio and nondimensional top flatness. Therefore, a uniform model of the boundary layer can be obtained to illustrate the effects of various riblet shapes.

Keywords: Riblet shapes; Boundary layer; Wall shear stress; Uniform model of the logarithmic law.

NOMENCLATURE

B	von Kármán's constants
F	surface roughness
h	riblet height
h^+	nondimensional height
h_0^+	characteristic riblet height
h_{pc}	cross-flow protrusion height
h_{pl}	longitudinal protrusion height
k	the reciprocal of κ
N_1	grid numbers
N_2	grid numbers
N_x	grid numbers in streamwise direction
N_y	grid numbers in normal direction
N_z	grid numbers in spanwise direction
s	riblet spacing
s^+	nondimensional spacing
u	mean velocity
u_τ	friction velocity
u^+	nondimensional velocity
$u^*_{\tau_t}$	wall shear velocity at the virtual origin
v	viscosity
y	normal distance of the wall
y^+	normal distance of the nondimensional wall
y_0	virtual origin
y_m	location of the maximum turbulent kinetic energy production
α	maximum velocity shift
ΔU^+	shift of the logarithmic law region
Δh^+	characteristic riblet height
κ	von Kármán's constants
τ_w	shear stress

1. INTRODUCTION

A riblet emulates the skin of fast-swimming sharks and has commercial value and resource conservation effect. A bionic riblet structure is formed by orderly arranged riblets (Dean B. *et al.* (2010)), which change the near-wall turbulent structure and decreases drag. Riblets have been widely used in ships, aerospace (Lee S.J. *et al.* (2005)), pipeline transportations (Vijiapurapu S. *et al.* (2007)), and wind turbine blades (Arndt R. *et al.* (2012); Zhao M. et al. 2017a, 2017b).

Many researchers from different fields investigated bionic riblets and drag reduction. Fluid dynamic experiments were performed in many successful works. For instance, Walsh *et al*. (1982) conducted

a hot wire experiment by using several longitudinal grooves; they found that various riblet shapes lead to drag reduction and can be expressed by nondimensional height h^+ and nondimensional spacing s^+.

$$h = \frac{hu}{\nu}, s = \frac{su}{\nu} \tag{1}$$

where h is the riblet height from bottom to top, s is the riblet spacing, $u_\tau = \sqrt{\frac{\tau_w}{\rho}}$ is the friction velocity based on wall shear stress τ_w, and ν is the viscosity. Park and Wallace (1994) used a single-sensor miniature hot wire probe to measure the velocity of symmetric V-shaped riblets in different locations, and they were able to obtain a drag reduction ratio of 4%. Kim *et al.* (2016) studied the hierarchical structure of nanostructures on microriblets; they found that the drag reduction mechanism involves the air-layer effect induced by nanometer structures and secondary vortex by microriblets.

Various riblet shapes were studied through computational fluid dynamics method (Huang W. *et al.* 2012, 2013). Launder and Li (1993) utilized a two-equation turbulence model to compare the V-, U-, and blade-shaped riblets with one another. Among the three shapes, the V-shaped riblets exhibited the best performance. Pollard *et al.* (1996) used control-volume finite-element simulation to simulate thin blade-shaped and V-shaped riblets; Their results indicated that riblets are required to ensure a thicker boundary layer than typical viscous laminar flow and the transient momentum exchanges between the inner and outer region motions that are associated with quasi-streamwise vortices must be minimized. Peet *et al.* (2008) employed the large eddy simulation for sine-shaped riblets, which performed better than straight riblets with respect to drag reduction.

Drag reduction mechanisms were studied at different aspects (Bacher E. and Smith C. 1985; Bechert D.W. and Bartenwerfer M. 1989; Pan J.Z. 1996). For instance, drag reduction is associated with turbulent boundary layers, and this association is reflected by velocity profiles. The logarithmic law layer for flat plate is described as follows:

$$u = k \ln y + B \tag{2}$$

$$u^+ = \frac{u}{u_\tau}, \quad y^+ = \frac{yu_\tau}{\nu}, \quad k = \frac{1}{\kappa} \tag{3}$$

where u^+ is the nondimensional velocity, y^+ is the normal distance of the nondimensional wall, u is the mean velocity, y is the normal distance of the wall, κ and B are the von Kármán's constants, and k is the reciprocal of κ. The general values of the von Kármán constants are defined as follows:

$$\kappa = 0.4 \sim 0.42, \quad B = 5.0 \sim 5.5 \tag{4}$$

The value of slope k is

$$k = 2.38 \sim 2.5 \tag{5}$$

Walsh *et al.* (1982) and Park and Wallace (1994) supported the von Kármán constants in Eq. (4) through hot wire experiments. Choi *et al.* (1993) , Boomsma and Sotiropoulos (2015), and Martin and Martin and Bhushan (2016) obtained the velocity profile for flat plate through simulations, which also supported the von Kármán constants in Eq. (4).

For the riblet surface, Choi *et al.* (1993) studied various mean velocity profiles normalized by wall shear rates. Sawyer and Winter (1987) presented a modified representation model where the velocity profile is defined as follows:

756 EMBED Equation.KSEE3 * MERGEFORMAT $u = \frac{1}{\kappa}\ln\frac{u(y-y)}{\nu} + B + F$ (6)

where y_0 is the virtual origin defined as $y = y - \frac{13\upsilon}{u}$, y_m is the location of the maximum turbulent kinetic energy production, $u^*_{\tau_t}$ is the wall shear velocity at the virtual origin, and F is the surface roughness parameter, which is a positive value for drag reduction cases. Tani (1988) found that F is associated with nondimensional riblet height. Aupoix *et al.* (2012) proposed the following expression of the logarithmic law:

$$u = \frac{1}{\kappa}\ln y + C + \Delta U \tag{7}$$

$$\kappa \approx 0.41 \text{◆} C \approx 5.2 \tag{8}$$

where ΔU^+ is the shift of the logarithmic law region caused by riblets. Through the study of six different V- and U-shaped riblets, the velocity shift was represented by the following parabola:

$$\Delta U = \alpha h (h - h) \tag{9}$$

where h is the characteristic riblet height, which separates the drag reduction from the rough regimes, and α is the maximum velocity shift. Bechert *et al.* (1997) proposed another expression, specifically,

$$\Delta U = 0.785 \Delta h \tag{10}$$

where Δh is the nondimensional protrusion height.

$$\Delta h = \frac{\Delta h u}{\nu}, \quad \Delta h = h - h \tag{11}$$

where Δh is the protrusion height, h_{pl} is the longitudinal protrusion height, and h_{pc} is the cross-flow protrusion height. Mayoral and Jiménez (2011) demonstrated that velocity profile shift has a similar function in logarithmic law:

$$\Delta U = \mu \Delta h, \quad \mu = 0.66 \tag{12}$$

The riblet velocity profile can be applied for improvement of wall function and turbulence models. By redefining the slope and intercept in the logarithmic law layer, the effect of riblets can be modeled for the reduction of calculation cost. In traditional perspectives, the intercept of the velocity profile in the logarithmic law layer is emphasized,

Table 1 Sizes of various riblet shapes

Model	Shape	R(mm)	s(mm)	h(mm)
29	V-shaped	——	0.51	0.25
37	Peak curvature	0.25	——	——
44	Valley curvature	0.12	0.51	0.25
45	Valley curvature	0.25	——	——
47	Valley curvature	0.20	0.51	0.25
51	Miscellaneous	——	0.51	0.25
52	Miscellaneous	——	1.02	0.25

and the reciprocal of the slope is set such that it is equal to von Kármán's constant. However, the entire velocity profile changes according geometric riblet shape. Therefore, we focused on determining the changing rules of intercept and slope that are related to the geometric parameters and riblet shapes.

The rest of this paper is organized as follows: the simulation methods are presented in Chapter 2, and the flow fields of various riblet shapes are described in Chapter 3. Then, drag change ratio, wall shear stress, and near-wall vorticity magnitude are analyzed. Analysis performed on the velocity profiles of various riblet shapes is presented in Chapter 4. A uniform model is proposed for the characterization of these profiles. Finally, conclusions are presented in Chapter 5.

2. SIMULATION METHODS

2.1 Computational Domain

The flow geometry is obtained through a three-dimensional computation, as shown in Fig. 1. A streamwise direction length of 2 m is required for complete development of the turbulence flow. The normal direction length is 0.5 m. The upper boundary has no effect on the turbulent boundary layer. Meanwhile, the inlet and upper boundaries are the velocity inlets, whereas the lower boundary is the flat plate or riblets. The outlet boundary is the outflow. The periodic boundary condition is used in the spanwise direction. The x, y, and z axes are the streamwise, normal, and spanwise directions, respectively.

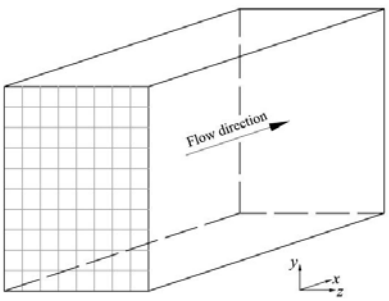

Fig. 1. 3D computational domain.

2.2 Riblets Geometry Model

Different riblet shapes contain the following riblet parameters: riblet height h, spacing s, and radius R. To compare with the experiments of Walsh *et al.* (1982), we selected seven different riblet shapes (Fig. 2), each with three geometric parameters, which are provided in Table 1.

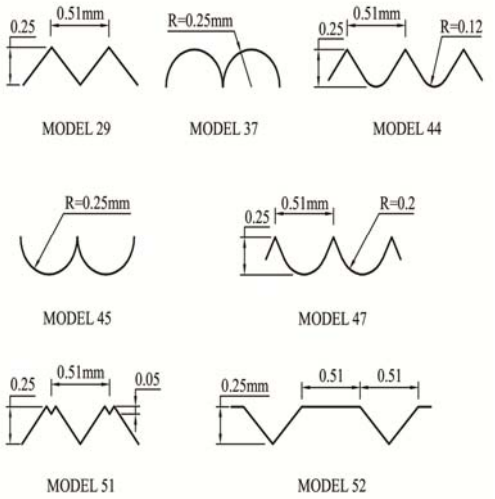

Fig. 2. Cross-sections of different riblet shapes.

2.3 Mesh Spacing

A structural mesh is used for the entire computational domain, as shown in Fig. 3. For Model 37, 0.05 mm is added to the geometric structure to adjust the mesh in the spanwise direction because the cross-section is the tangent of the curve. The meshes are refined such that $y^+ \approx 1$ at the first layer grid height. To validate the mesh independence, two sets of grid numbers (N_1 and N_2) for one riblet are provided in Table 2, where N_x is the streamwise direction, N_y is the normal direction, and N_z is the spanwise direction. The results of grid numbers N_1 and N_2 show no apparent difference, as shown in Figs. 4, 5 and 6, and the starting position is at $y = 0$ in the normal direction, that is, the bottom of the riblets. Therefore, the independent grid is validated, and then the fine $N2$ meshes are adopted in the subsequent tests.

2.4 Numerical Method

Renormalization group (RNG) k-epsilon is used along with enhanced wall function turbulence models (Huang W. *et al.* 2015, 2017). An all-speed Roe scheme (Li X.S. *et al.* 2014, 2016; Ren X.D. *et al.* 2017) developed from the preconditioned Roe scheme (Huang D.G. *et al.* 2006, 2007, 2008) is

Table 2 Grid parameters

Type	$N = N \times N \times N$	Mesh number (billion)	$N_2 = N_x \times N_y \times N_z$	Mesh number (billion)
Flat plate	201×76×6	0.11	——	——
Model 37	201×65×9	0.14	501×91×14	0.65
Model 44	201×51×8	0.09	501×101×12	0.65
Model 45	201×71×10	0.18	501×101×12	0.75
Model 47	201×51×8	0.12	501×101×12	0.65
Model 51	201×51×10	0.11	501×101×14	0.76
Model 52	201×51×14	0.15	501×101×22	1.10

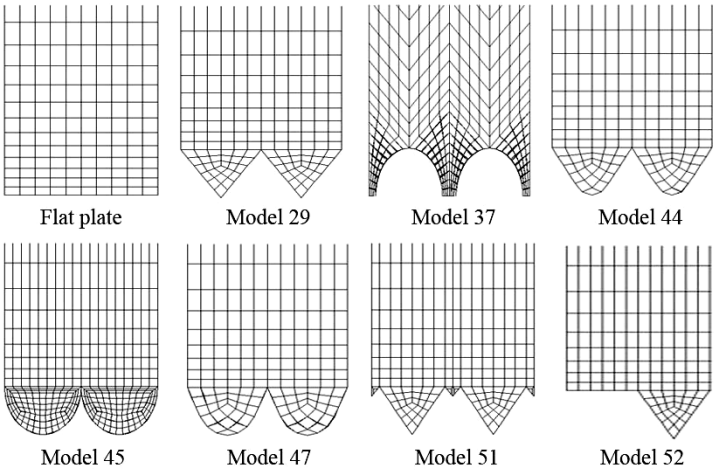

Fig. 3. Details of the mesh for the flat plate and various riblet shapes.

adopted in the discretization Navier-Stokes equations along with weighted essentially non-oscillatory reconstruction methods (Su X.R. *et al.* 2013a, 2013b, 2013c) for high-order accuracy.

3. Flow Field Of Various Riblet Shapes

3.1 Drag Change Ratio

The extents of drag reduction in various riblet shapes were compared with the experimental results (Walsh M.J. 1982) in Figs. 4–6. The riblet drag effect was indicated by the drag change ratio defined as $D = \frac{\Delta D}{D} = \frac{(D - D)}{D}$, where D_R is the drag of the riblets, and D_F is the drag of the flat plate. When the drag change ratio was negative, the drag decreased.

The simulation results were consistent with the experiments. The drag change ratio generally increased with h^+, except in Model 51. In Models 44, 45, 47, and 52, the drag change ratios changed significantly in the entire h^+ range. Models 44, 45, and 47 showed significant drag reduction at low h^+, whereas the decrease in the drag of Model 52 was negligible. In Models 29, 37, and 51, the ratios changed slightly in the entire h^+ range. Models 29 and 51 showed drag reduction effects in the same range. Drag in Model 37 increased with h^+.

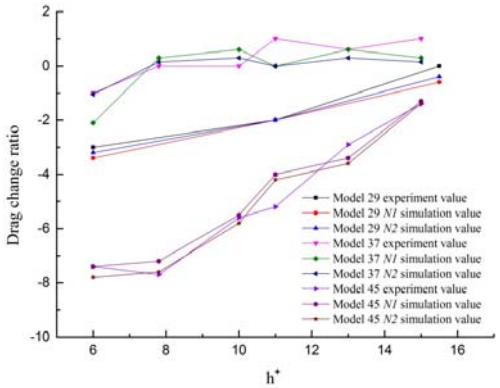

Fig. 4. Drag change ratio of Models 29, 37, and 45.

The flow fields of various riblet shapes were analyzed in the next sections. The inlet velocity was set to 7.5 m/s and thus h^+ was 6. The cross-section was set to 1.5 m at the streamwise direction.

The wall shear stress of flat plate is uniform at the spanwise direction, whereas the various riblet

shapes are not. The cross-sections of the various riblet shapes presented different wall shear stress distributions. The low wall shear stress region is defined as the region where the wall shear stress is less than or equal to the flat plate, whereas the high wall shear stress region.

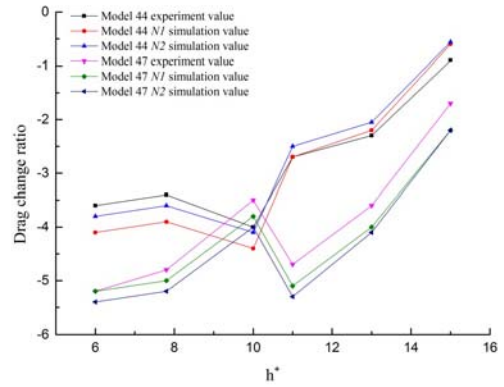

Fig. 5. Drag change ratio of Models 44 and 47.

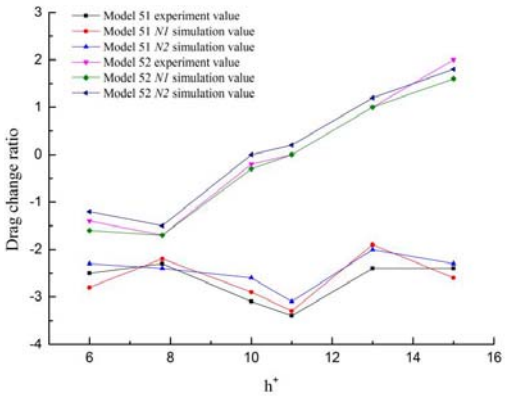

Fig. 6. Drag change ratio of Models 51 and 52.

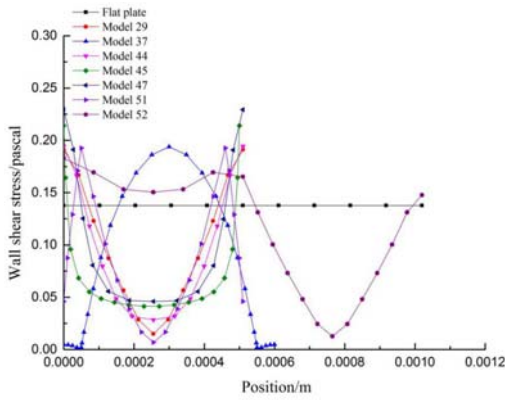

Fig. 7. Wall shear stress distribution.

3.2 Wall Shear Stress

Figure 8 shows the contours of the wall shear stress. The high wall shear stress region was located at the top of the riblet, whereas the low wall shear stress region was situated near the bottom of the riblet. The wall shear stresses of the flat plate and riblets had no uniform distribution at the streamwise direction. The wall shear stress decreased when the length of the streamwise direction increased. The entrance of the wall shear stress was larger than the other regions at the streamwise direction because the inlet velocity influenced the entrance. The wall shear stress of flat plate was uniform at the spanwise direction, whereas those of the riblets were not. The wall shear stresses of the riblets varied with riblet shape.

3.3 Near Wall Vorticity Magnitude

The contours in Fig. 9 reflect the near-wall vorticity magnitudes of the flat plate and the various riblet shapes. The near-wall location was at $y^+ \approx 50$. The vorticity magnitude of the flat plate was uniform at the spanwise direction, whereas that of the riblet was not. The vorticity magnitude value of the flat plate was initially high at normal distance. The vorticity magnitude of the flat plate started to decrease when normal distance increased. The state of riblets vorticity magnitude was the process from low in the bottom of the riblets to high with the normal distance increasing, and reaches the maximum values near the top and then reduces.

3.4 Two Geometry Factors REflecting Riblet Characteristics

The above discussions indicate that the wall shear stresses of riblets are closely related with the cavity volume, which reflects the low wall shear stress region, and tip shape, which reflects the high wall shear stress region. Therefore, two nondimensional geometry parameters, namely, the cavity ratio α^+ and top flatness β^+, are defined as follows:

$$\alpha^+ = \frac{V_R}{V_W} \tag{13}$$

$$\beta = \frac{\beta}{90} \tag{14}$$

where V_R is the cavity volume filled with fluids, V_W is the cavity volume that includes the wall, and β is the averaged angle of the top 20% height, as shown in Fig. 10.

4. BOUNDARY LAYER AND MODEL

4.1 Velocity Profile

The velocity profiles were analyzed by obtaining the cross-section at 1.5 m at the streamwise direction for the evaluation of different riblet shapes on the turbulent boundary layer. Figures 11–14 illustrate the velocity profiles of the flat plate and riblets at various velocities. In the four figures, the starting position is at $y = 0$ at the normal direction, which is located at the bottom of the riblets. The velocity and the wall shear stress are the mean values.

The velocity profiles of the flat plate and Model 29 are shown in Fig. 10. The velocity profile of the flat plate is expressed by $u^+ = y^+$ at the viscous sublayer region and by Eq. (2) at the logarithmic law region.

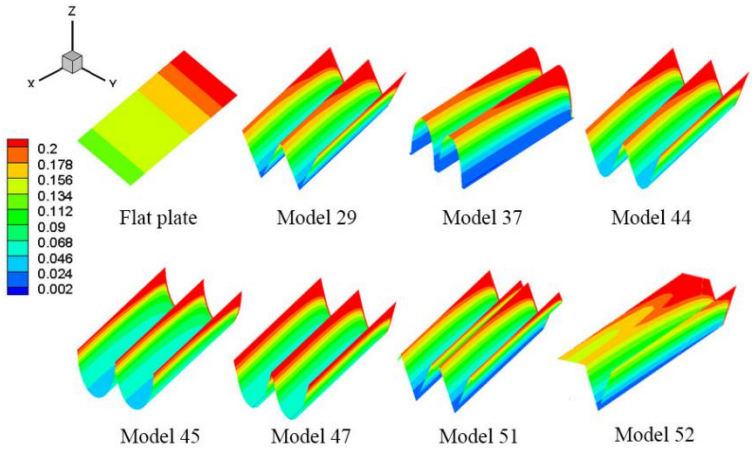

Fig. 8. Contours of the wall shear stress.

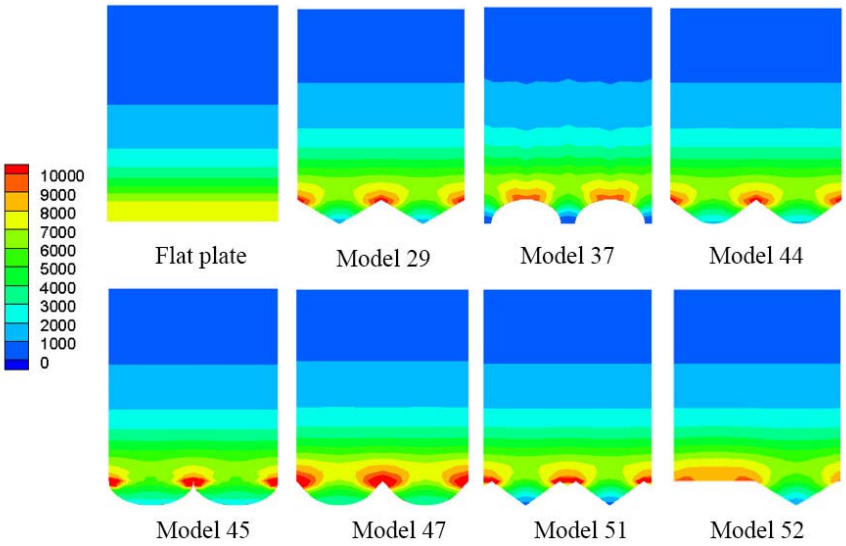

Fig. 9. Contours of the near wall vorticity magnitude.

The velocity profiles of the riblets are different from that of the flat plate. The reciprocals of the slopes and intercepts exhibited more considerable differences than von Kármán's constants in various free stream velocities, which is different from the traditional perspective of the riblet model on logarithmic law that only modifies the intercept, as shown in Eq. (7). The maximum and minimum values of the fitting straight lines were indicated in the four figures. As proposed in Ref. (Yu Y. *et al.*), the effect of free stream velocity can be modeled as the nondimensional geometric parameter h^+.

Moreover, the velocity profiles of the various riblet shapes were different from each other in the logarithmic law region. The riblet shape factor had a greater effect on the slopes and intercepts than the free stream velocity factor. In the following section, an surprising model that can uniformly consider the riblet shapes was proposed.

4.2 Uniform Model for the logarithmic law layer of riblets

The relationship between the slopes and intercepts of various riblet shapes with h^+ are illustrated in Figs. 15–16. The slope and intercept of various riblet shapes were different from each other. The slope increases with h^+, whereas the intercept exhibited an opposite behavior. The slope and intercept were also changed by shape factors.

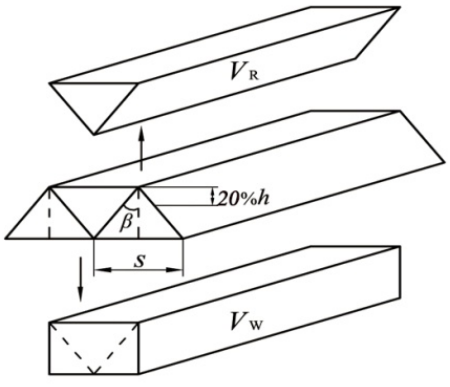

Fig. 10. Schematic of the riblet characteristics.

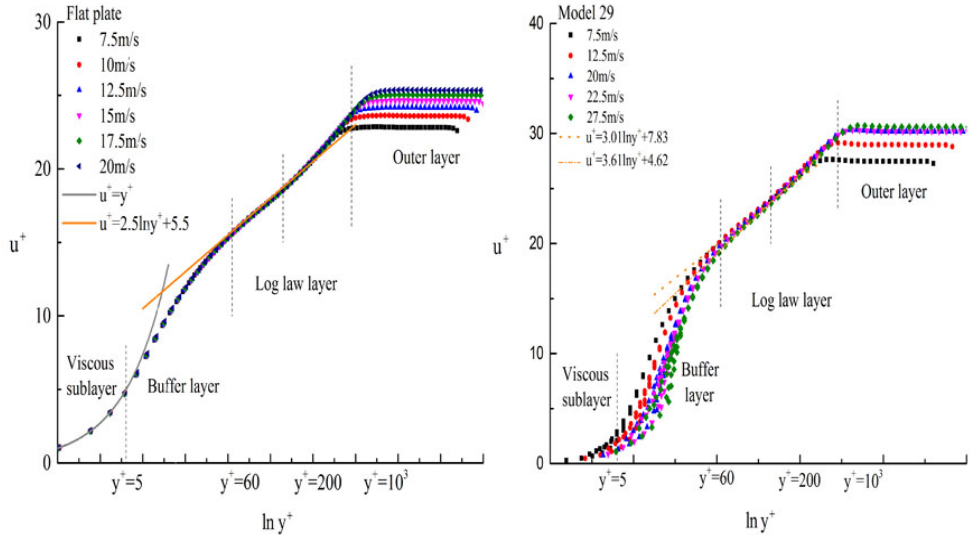

Fig. 11. Velocity profiles of the flat plate and Model 29.

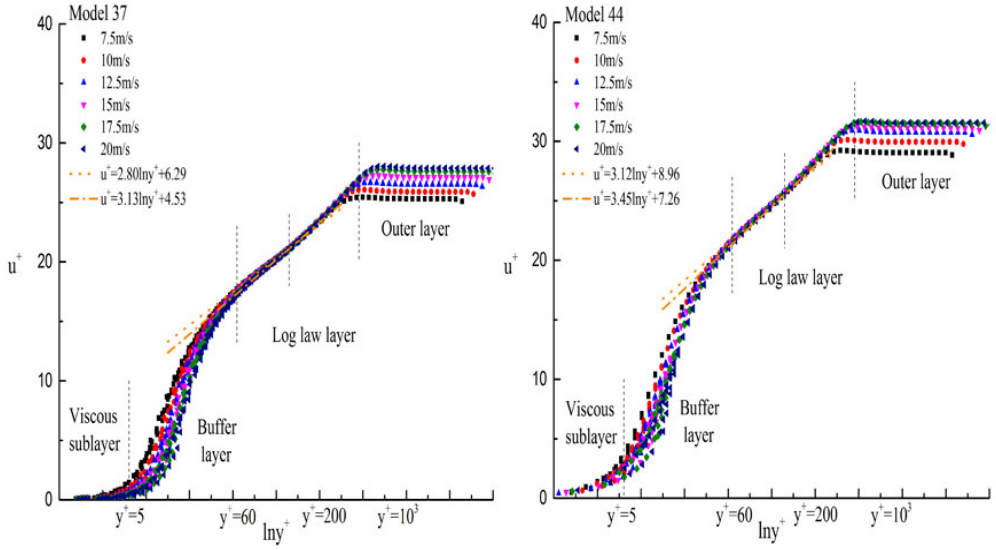

Fig. 12. Velocity profiles of Models 37 and 44.

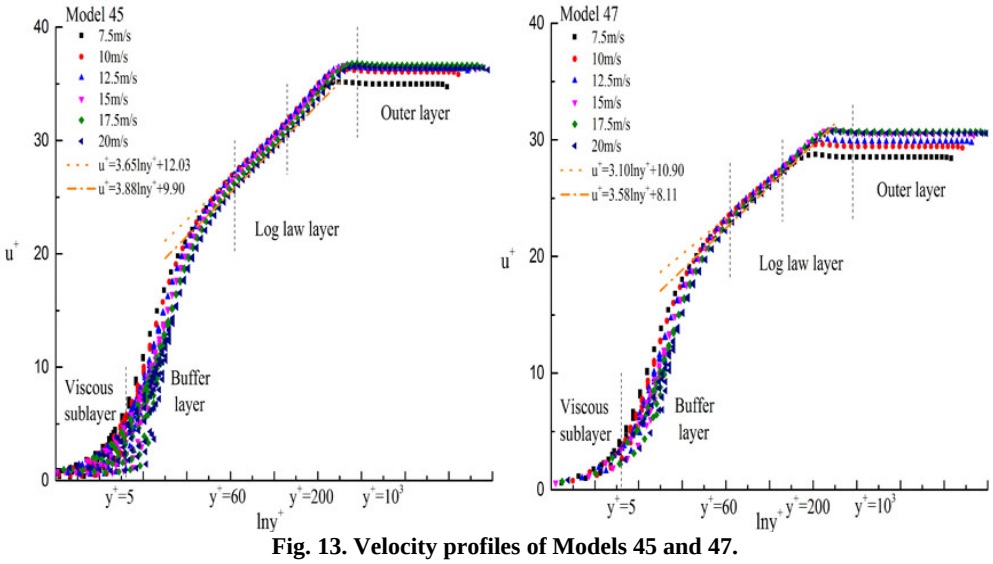

Fig. 13. Velocity profiles of Models 45 and 47.

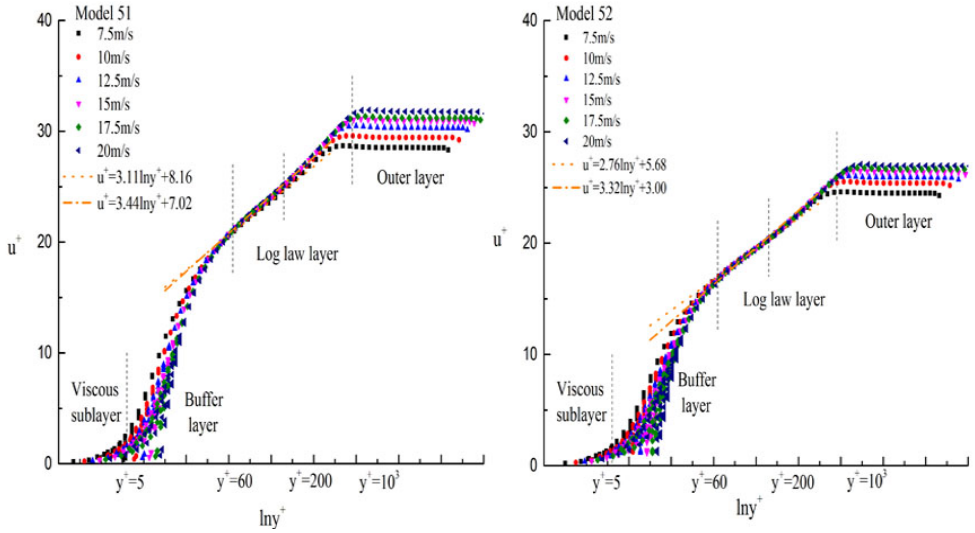

Fig. 14. Velocity profiles of Models 51 and 52.

To describe the change rules uniformly, we defined a shape factor on the basis of two nondimensional geometry parameters α^+ and β^+ of Eqs. (13) and (14) as follows:

$$T = \sqrt{\frac{\alpha}{\beta}} \tag{15}$$

where T^+ is the nondimensional shape factor, α^+ is the nondimensional cavity ratio, and β^+ is the nondimensional top flatness.

Slope k and intercept B in Eq. (2) are related to h^+. Two functions are defined as a linear function as follows:

$$k = m_1 h^+ + m_0 \tag{16}$$

$$B = n_1 h^+ + n_0 \tag{17}$$

where m_1 and m_0 are the function coefficients of the slope, and n_1 and n_0 are the function coefficients of the intercept.

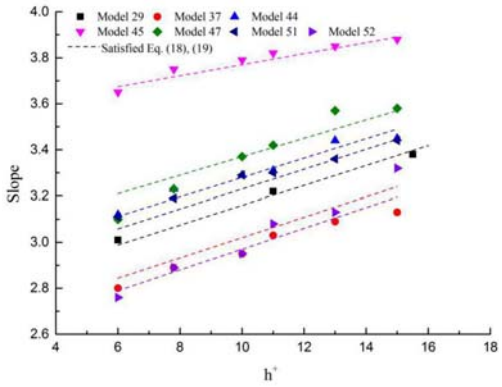

Fig. 15. Relationship between slope and h^+.

The coefficients of the functions are related to shape factor T^+. The formula for the quadratic function is as follows:

$$m_1 = 0.026\left(T^+\right)^2 - 0.083\left(T^+\right) + 0.10 \tag{18}$$

$$m_0 = 0.896\left(T^+\right)^2 - 0.440\left(T^+\right) + 2.302 \tag{19}$$

$$n_1 = -0.705\left(T^+\right)^2 + 1.448\left(T^+\right) - 0.936 \tag{20}$$

$$n_0 = 6.402\left(T^+\right)^2 - 2.645\left(T^+\right) + 5.409 \tag{21}$$

Various riblet shapes possess significant values for the analysis of the turbulent boundary layer. The von Kármán constants are redefined by Eqs. (16) and (17). The slope and intercept are uniformly described by Eqs. (18)–(21). Basing on a simple shape factor T^+, we proposed a uniform model for the boundary layers of various riblet shapes.

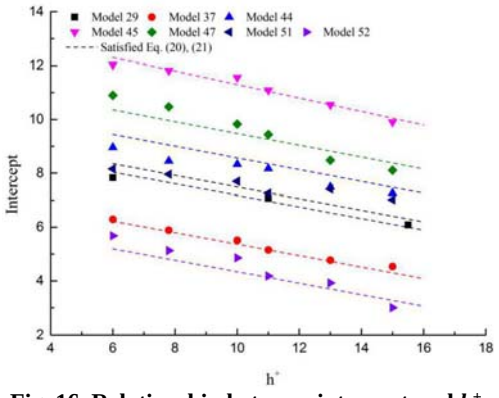

Fig. 16. Relationship between intercept and h^+.

5. CONCLUSION

Various riblet shapes were numerically simulated by using the RNG turbulence model and analyzed on the basis of the turbulent boundary layer. The following conclusions were obtained:

(1) The slope and intercept of the logarithmic law are not constant in the boundary layers of the riblets, which are affected by nondimensional geometric parameters and riblet shapes.

(2) A shape factor is defined with the cavity ratio and top flatness, which can emulate riblet shape characteristics.

(3) Based on the shape factor, an improved model for redefining the slope and the intercept is proposed. It can uniformly describe the effect of riblet shapes.

ACKNOWLEDGEMENTS

This study is supported by the Projects 51736008 and 51276092 of the National Natural Science Foundation of China.

REFERENCES

Arndt, R., L. Chamorro and F. Sotiropoulos (2012). Drag reduction in large wind turbines through riblets: evaluation of different geometri-es. *50th AIAA Aerospace Sciences Meeting include the New Horizons Forum and Aerospace Exposition, 09-12 January 2012, Nashville, Tennessee*.

Aupoix, B., G. Pailhas and R. Houdeville (2012). Towards a general strategy to model riblet effects. *AIAA Journal*, 50(3), 708-716.

Bacher, E. and C. Smith (1985). A combined visualization-anemometry study of the turbulent drag reducing mechanisms of triangular micro-groove surface modificati-ons. *American Institute of Aeronautics and Astronautics, Shear Flow Control Conference, Boulder, CO, Mar. 12-14, 1985, 85-0548. 11 p. USAF-supported research.* (Vol.-1).

Bechert, D. W., & M. Bartenwerfer (1989). The viscous flow on surfaces with longitudinal ribs. *Journal of Fluid Mechanics*, 206(1), 105-129.

Bechert, D. W., Bruse, M., Hage, W., Van, d. H. J. G. T., and Hoppe, G. (1997). Experiments on drag-reducing surfaces and their optimization with an adjustable geometry. *Journal of Fluid Mechanics*, 338, 59-87.

Boomsma, A. and Sotiropoulos, F. (2015). Riblet drag reduction in mild adverse pressure gradients: a numerical investigation. *International Journal of Heat and Fluid Flow* 56, 251-260.

Choi, H., P. Moin, and J. Kim (1993). Direct numerical simulation of turbulent flow over riblets. *Journal of Fluid Mechanics* 255, 503-539.

Dean, B. and B. Bhushan (2010). Shark-skin surfaces for fluid-drag reduction in turbulent flow: a review. *Philosophical Transactions of the royal society A*, 368, 4775-4806.

Huang, D. G., H. Y. Ke and J. Y. Du (2008). A set of new general united fluid dynamic equations for arbitrary equation of state. *Journal of Mechanical Engineering Science* 222(5), 958-995.

Huang, D. G. (2006). Unified computation of flow with compressible and incompressible fluid based on roe's scheme. *Applied Mathematics and Mechanics*, 27(6), 758-763.

Huang, D. G. (2007). Preconditioned dual-time procedures and its application to simulating the flow with cavitations. *Journal of Computational Physics*, 223(2), 685-689.

Huang, W., L. Q. Li, X. Q. Chen and L. Yan (2017). Parametric effect on the flow and mixing properties of transverse gaseous injection flow fields with streamwise slot: a numerical study. *International Journal of Hydrogen Energy* 42, 1252-1263.

Huang, W., S. B. Li, L. Yan and Z. G. Wang (2013). Performance evaluation and parametric analysis on cantilevered ramp injector in supersonic flows. *Acta Astronautica* 84(3), 141-152.

Huang, W., W. D. Liu, S. B. Li, Z. X. Xia, J. Liu and Z. G. Wang (2012). Influences of the turbulence model and the slot width on the transverse slot injection flow field in supersonic flows. *Acta Astronautica* 73(2), 1-9.

Huang, W., J. G. Tan, J. Liu and L. Yan (2015). Mixing augmentation induced by the interaction between the oblique shock wave and a sonic hydrogen jet in supersonic flows. *Acta Astronautica* 117, 142-152.

Kim, T., R. Shin, M. Jung, J. Lee, C. Park and S. Kang (2016). Drag reduction using metallic engineered surfaces with highly ordered hierarchical topographies: nanostructures on micro-riblets. *Applied Surface Science* 367, 147-152.

Launder, B. E. and S. P. Li (1993). On the prediction of riblet performance with engineering turbulence models. *Journal of Applied Scientific Research* 50(3-4), 283-298.

Lee, S. J. and Y. G. Yang (2005). Control of flow around a NACA0012 airfoil with a micro-riblet film. *Journal of Fluids and Structures* 20(5), 659-672.

Li, X. S. (2014). Uniform algorithm for all-speed shock-capturing schemes. *International Journal of Computational Fluid Dynamics* 28(6-10), 329-338.

Li, X. S. and X. L. Li (2016). All-speed Roe scheme for the large eddy simulation of homogeneous decaying turbulence. *International Journal of Computational Fluid Dynamics* 30(1), 69-78.

Martin, S. and B. Bhushan (2016). Fluid flow analysis of continuous and segmented riblet structures. *The Royal Society of Chemistry* 6(13), 10962-10978.

Mayoral, R. and J. Jiménez (2011). Drag reduction by riblets. *Philosophical Transactions of the royal society A*, 369, 1412-1427.

Pan, J. Z. (1996). Experimental exploration on the new concept of turbulent drag reduction.

Journal of Aerodynamics 14(3), 304-310.

Park, S. R. and J. M. Wallace (1994). Flow alteration and drag reduction by riblets in a turbulent boundary layer. *AIAA Journal*, 32(1), 31-38.

Peet, Y., P. Sagaut and Y. Charron (2008). Turbulent drag reduction using sinusoidal riblets with triangular cross-section. *AIAA 38th Fluid Dynamic Conference and Exhibit. June 23-26 2008, Seattle, WA*.

Pollard, A., S. Tullis, X. Wang and A. M. Savill (1996). Simulating turbulent flow over thin element and flat valley v-shaped riblets. *AIAA Journal* 34(11), 2261-2268.

Ren, X. D., C. W. Gu and X. S. Li (2017). Role of the momentum interpolation mechanism of the roe scheme in shock instability. *International Journal for Numerical Methods in Fluids* 84, 335–351.

Sawyer, W. G. and K. G. Winter (1987). An investigation of the effect on turbulent skin friction of surfaces with streamwise grooves. *Proceedings of the International Conference, London, England. 1987, 330A-3362*.

Su, X., D. Sasaki and K. Nakahashi (2013). Cartesian mesh with a novel hybrid WENO/meshless method for turbulent flow calculations. *Computers and Fluids* 84(18), 69-86.

Su, X., S. Yamamoto and K. Nakahashi (2013). Analysis of a meshless solver for high Reynolds number flow. *International Journal for Numerical Methods in Fluids* 72(5), 505-527.

Su, X., S. Yamamoto and X. Yuan (2013). On the Accurate Prediction of Tip Vortex: Effect of Numerical Schemes. *ASME Turbo Expo 2013: Turbine Technical Conference and Exposition, San Antonio, GT2013-94660.*

Tani, I. (1988). Drag reduction by riblet viewed as roughness problem. *Proceedings of the Japan Academy*, 64(2), 21-24.

Vijiapurapu, S. and J. Cui (2007). Simulation of turbulent flow in a ribbed pipe using large eddy simulation. *Numerical Heat Transfer Part A: Applications* 51(12), 1137-1165.

Walsh, M. (1982). Turbulent boundary layer drag reduction using riblets.; Riblets as a viscous drag reduction technique. *AIAA 20th Aerospace Sciences Meeting, January 11-14, 1982, Orlando Florida*.

Yu, Y., M. M. Zhang and X. S. Li (2018). Numerical investigation of v-shaped riblets and an improved model of riblet effects. *Proceedings of the Institution of Mechanical Engineers Part C: Journal of Mechanical Engineering Science*.

Zhao, M., M. Zhang and J. Xu (2017). Analysis of flow transition effects on the performances of a wind power heat pump system. *Applied Thermal Engineering* 123, 1318-1326.

Zhao, M., M. Zhang and J. Xu (2017). Numerical simulation of flow characteristics behind the aerodynamic performances on an airfoil with leading edge protuberances. *Engineering Applications of Computational Fluid Mechanics* 11(1), 193-209.